Versatile Gold-Polymer Nanointerfaces Probed by GISAXS

Murtaza Bohra,[1, 2] Arun Showry,[2] Panagiotis Grammatikopoulos,[1] and Vidyadhar Singh[1, 3]*

[1]*Nanoparticles by Design Unit, Okinawa Institute of Science and Technology Graduate University, 1919-1 Tancha Onna-Son, Okinawa 904-0495, Japan*
[2]*Mahindra Ecole Centrale, Survey Number 62/1A, Bahadurpally Jeedimetla, Hyderabad 500043, Telangana, India*
[3]*Department of Physics, Jai Prakash University, Chapra, 841301 Bihar, India*

Abstract

An increasing trend toward integration of polymers in microelectronics and organic electronics has recently boosted research focusing in metal-polymer interfaces. These two materials differ vastly, with the former forming dense, crystalline, cohesive structures and the latter forming open structures bound together by weak van der Waals forces. As a result, there is dire need to assess their surface features (e.g., roughness) and correlate them with corresponding growth parameters, as metal-polymer interfaces are mainly determined by the preparation process. Here, we report a laboratory-based grazing-incidence small-angle x-ray scattering (GISAXS) study on distinct gold-polymer interfaces fabricated with different growth mechanisms, utilizing in-plane and oblique sputter geometries. GISAXS provided an improved analytic scheme for the buried surface in free-standing 2D gold-polymer nanosheets (with 19% porosity) revealing their fractal structure (Porod slope: -1.71). Two quantitative approaches (Height-Height Correlation and Power Spectral Density functions) were used to describe rough surfaces characterized by Atomic Force Microscopy (AFM) in consort with GISAXS data; different correlation length dependencies on growth time were revealed for gold rough surfaces grown on bare and polymerized Si. The results are considered pertinent to interfacial nanoscience and engineering, enabling statistical data collection from large surface areas, in a fast and nondestructive manner.

Introduction

With a spurt of activity in the area of wearable/stretchable electronics [1-2], 3D/2D printing for greater functionality [3] and bio-inspired activity [4-5], manipulation of gold-polymer nanointerfaces is a central concept with respect to interactions responsible for transpiring surface-driven phenomena [1-7]. A fully stretchable and highly durable new type of triboelectric nanogenerators based on gold nanosheets embedded into a polymer matrix [1-2] was recently proposed for self-powered human-motion detectors with customizable functionality. Minnai et al. [8] have reported that mechanical stretching of gold nanocluster-polymer nanocomposite films can induce a simultaneous and controllable modulation of the

optical and electrical properties [1-2, 9]; this can be the basis of next-generation wearable/portable electronics and deformable optics. Remarkably, the controlled and reversible shape transformation of 2D gold/polymer nanosheets into 1D nanoscrolls in response to variation in pH value of the surrounding medium was previously demonstrated [10]. Because of their large surface area and loading capacity, these two-way shape-changing materials (i.e., nanosheets and nanoscrolls) can be used for future smart drug-delivery vehicles. More recently, a novel nanoplasmonic-based antibacterial polymer film consisting of anisotropic gold nanorods and organic dye [4] offered the capability of killing Gram-negative bacteria on its surface when exposed to white light; its anticipated application is for sterilization of surfaces in hospital environments. In view of these groundbreaking applications, it is imperative to understand the formation of gold-polymer nano-surfaces and interfaces and their structure-property correlation, which is the key factor in evaluating the performance of nanoscale devices. Though exfoliation of free-standing gold nanostructures from underlying substrates [1-2, 10-12] and the basic growth kinetics of gold nanostructures [13-15] are reasonably well understood, in-depth growth studies of rough gold nanointerfaces are still scarce.

Whilst a vast arsenal of characterization techniques is available for analyzing nanointerfaces, many still suffer from inherent weaknesses such as destructive sample preparation and limited-area scanning capability [14-15]. In contrast, grazing incidence small-angle X-ray scattering (GISAXS) is a powerful method which provides averaged statistical information over the entire illuminated/sampled area, as well as the ability to access buried nanostructures located well below the surface that are hard to access by local real-space techniques. GISAXS experiments generally require both high primary beam intensity and low beam divergence; thus, until now, most experiments have been performed at dedicated synchrotron facilities [14-18]. In recent years, however, the GISAXS technique has also become available using non-synchrotron lab equipment thanks to the development of brilliant X-ray sources, precise optics, and sensitive detectors. Recent studies show that GISAXS can develop further into an excellent technique for the investigation of embedded nanostructures in 3D-printed and many other technically relevant 2D films [3, 19-21].

Our current study involves laboratory-based GISAXS exclusively, which enables the investigation of growth kinetics of various gold-polymer interfaces and free-standing flat gold nanosheets with high statistical relevance. Combining GISAXS and Atomic Force Microscopy (AFM), we identify the main growth regimes and their thresholds, which is crucial for nanostructure tailoring. The synergy between autocorrelation-based surface-roughness approaches (from AFM data) and Guinier and Porod approximations for deducing critical surface parameters (from GISAXS data) paves the way to model the behavior of various gold-polymer nanointerfaces for numerous potential applications.

Experimental

A. Growth of Gold-Polymer Nanointerfaces

Gold nanostructures were grown on bare Si, and polymer (branched polyethyleneimine; bPEI) coated Si substrates, via conventional DC-sputtering at ambient temperature. In top-down sputtering geometry, the substrate-target distance was fixed at 5 cm. Gentle growth conditions (low DC power, 4 W; short growth time span, 10–120 s; and working gas pressure, 7×10^{-3} mbar) were chosen to study the initial growth regime. The thin polymer layer was coated on a Si (100) wafer by spin-coating (MS–A–150, MIKASA, Japan) at 3,000 rpm for 30 s. The polymer solution was prepared by mixing 25 µL of 50 % bPEI solution (MW 25 k Da, Sigma–Aldrich, St. Louis, US) in 225 µL of methanol solution, and slowly dispensed onto the pre-cleaned Si (100) wafer as described elsewhere [10]. The oblique (at 89° angle) gold deposition was also carried out while maintaining other in-plane sputter conditions. A MultiMode AFM (Bruker, CA) was used to acquire real-space AFM data in tapping mode.

B. All Angle X-Ray Scattering Measurements

Gold-polymer nano-interfaces were investigated by all angle X-ray scattering, as described in Fig. 1, by mapping in reciprocal space. According to this methodology, a well-collimated incident X-ray beam of wave vector k_i ($|k|=2\pi/\lambda$) is kept at a small grazing angle with respect to the sample surface in order to enhance the near-surface scattering. The incident angle α_i is generally selected close to the angle of total external reflection α_c $(0 < \alpha_i \leq 4.5^o)$. The incident X-ray beam is scattered by nanostructures on the surface along k_f directions, determined by out-of-plane and in-plane angles, α_f and $2\theta_f$, respectively. The scattering wave vector $q=k_f - k_i$, is composed of vector components q_x, q_y, and q_z related to the experimental angles by Equation (1) [14-15];

$$q = \frac{2\pi}{\lambda}\begin{pmatrix} Cos(\alpha_f)Cos(2\theta_f) - Cos(\alpha_i) \\ Cos(\alpha_f)Sin(2\theta_f) \\ Sin(\alpha_f) + Sin(\alpha_i) \end{pmatrix} = \begin{pmatrix} q_x \\ q_y \\ q_z \end{pmatrix} \qquad \text{Eq. (1)}$$

For the assigned coordinate system, the *x*-direction is parallel to the sample surface and the grazing incident beam, the *y*-direction is parallel to the sample surface and perpendicular to the incident beam, whilst the *z*-direction is perpendicular to the sample surface. Yoneda [14-15] revealed a surface reflection of X-rays at low angles close to the critical angle, $\alpha_f(\alpha_{\text{Yoneda}}) = \alpha_c$.

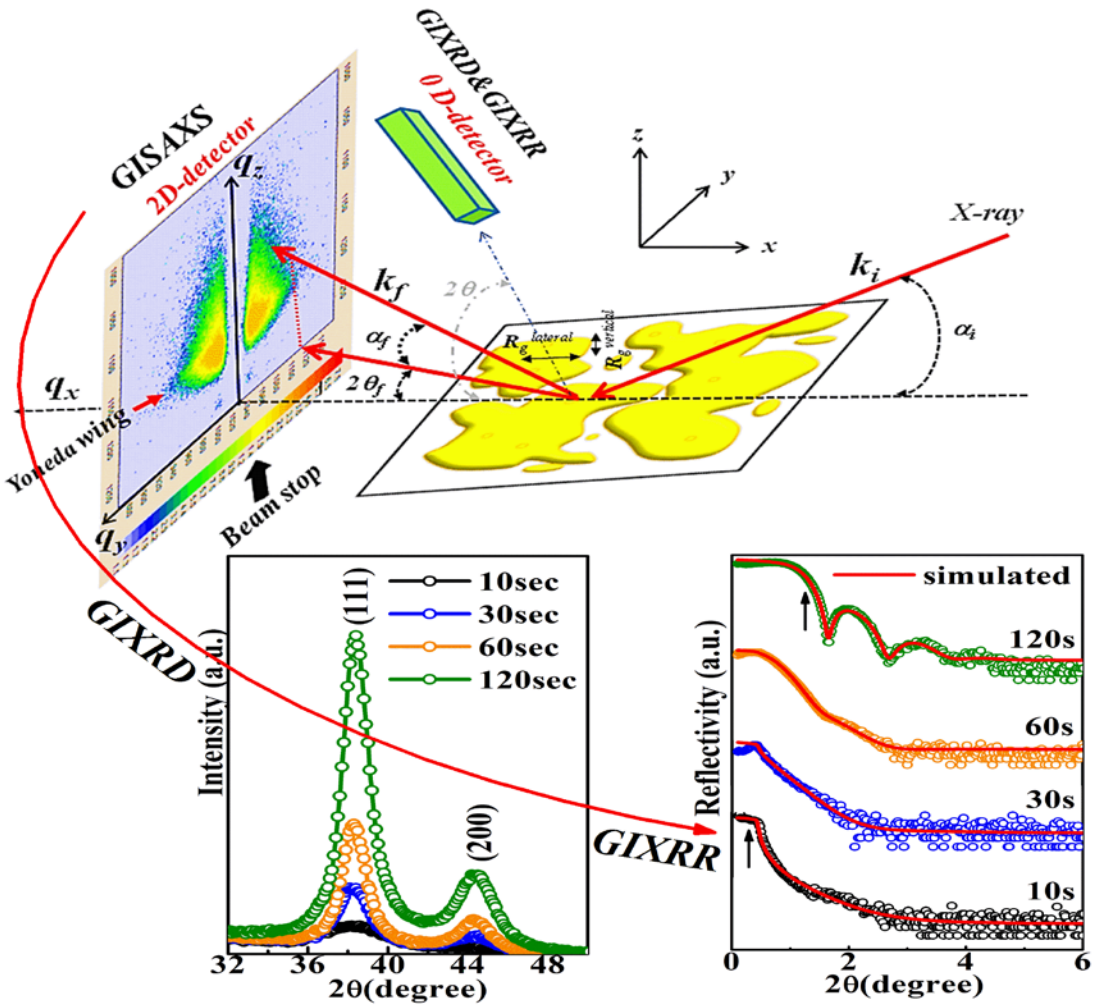

Figure 1: *All angle x-ray scattering geometry* (*GISAXS, GIXRR and GIXRD*), *under grazing incidence condition.* k_i *is the wave vector of the incident x-ray beam,* k_f *is the wave vector of the outgoing X-ray beam, and* q ($=k_f - k_i$) *is the scattering wave vector, with components* q_x, q_y, *and* q_z *which are related to scattering angles* (α_f, $2\theta_f$, *and* α_f). *The Yoneda wing is due to a fraction of the incident beam which travels within the surface as an evanescent wave and emerges at the far edge of the sample at the critical angle,* $\alpha_f(\alpha_{\text{Yoneda}}) = \alpha_c$. *More details can be found in the main text.*

The physical scattering and interference processes differ significantly within this family of X-ray techniques. For all small scattering angles, the scattering vector q is also small, typically between 0 and 1 nm^{-1}, and hence relatively large dimensions are probed in real space (~ 6–600 nm). X-ray reflectivity (GIXRR) in the specular geometry probes the density profile perpendicular to the surface, and in the off-

specular geometry large lateral electron density correlations (along q_x). The GISAXS configuration, on the other hand, probes the morphology parallel to the surface (along q_y) and perpendicular to it (along q_z), at intermediate length scales (typically between a few nm and a few hundreds of nm). Therefore, the presence of nanoscale inhomogeneity, electron density variation, and surface roughness can be easily investigated. In the case of wider angle scattering (typically > 10°), the scattering centers are the atoms; the related technique is grazing incidence X-ray diffraction (GIXRD), which allows probing the crystallographic lattices of nanostructures.

All X-ray data were collected using a Bruker D8 Discover XRD^2 system with Cu K_α X-ray source (operated at 40 kV and 40 mA). GISAXS intensity spectra were collected by a 2D VÅNTEC-500 detector with 900 s exposure time, containing 2048 × 2048 pixels and positioned perpendicular to the incident beam at a distance of 30 cm from the sample. An Al beam-stop was placed vertically in front of the detector to prevent overflow of surface scattering in the specular plane, and to enable better resolution of the diffuse part of the scattering in the off-specular plane for analyzing the contribution of nanostructures. The GIXRD (α_f & $2\theta_f = 0^o - 90^o$) and GIXRR ($\alpha_f = 0^o - 3^o$ & $2\theta_f = 0^o$) measurements were performed in the reflectivity plane placing a 0D-scintillator detector in the k_f direction. GIXRD results described that gold nanostructures preserve their cubic (FCC) symmetry even at the early stage of growth, while with their subsequent growth, a vertical correlation could be observed with [111] facets. The thickness calculated from GIXRR data increases from 1.2 to 7.2 nm with growth time. The surface roughness, on the other hand, shows a rapid increase (0.66 – 2.27 nm) with growth time 10 – 60 s, but at long deposition times (120 s) it falls sharply (0.8 nm) again.

Results and Discussion

A. GISAXS ($\alpha_f = 0^o$- 6^o & $2\theta_f = -3^o$ to $+3^o$) and AFM for In-Plane Deposition.

i) Qualitative Analysis

In this part of the study, initial growth regimes of gold nanostructures are qualitatively analyzed to understand essential morphological and spatial distribution variations with growth time (0 – 120 s). Fig. 2(a–c) and 2(d–f) show how the reciprocal space GISAXS and real space AFM patterns evolve with the progression of gold deposition on bare and polymer-coated Si wafers, respectively. The GISAXS pattern represents maps of scattered intensities in the given in-plane ($q_y \simeq |k| 2\theta_f$) and out-of-plane ($q_z = |k|\alpha_f$) scattering range. A GISAXS pattern of a bare Si and polymer coated Si (shown in the Supporting Information, Figure S1) shows hardly any discernible particle scattering. However, several prominent features start evolving with the proceeding of gold deposition.

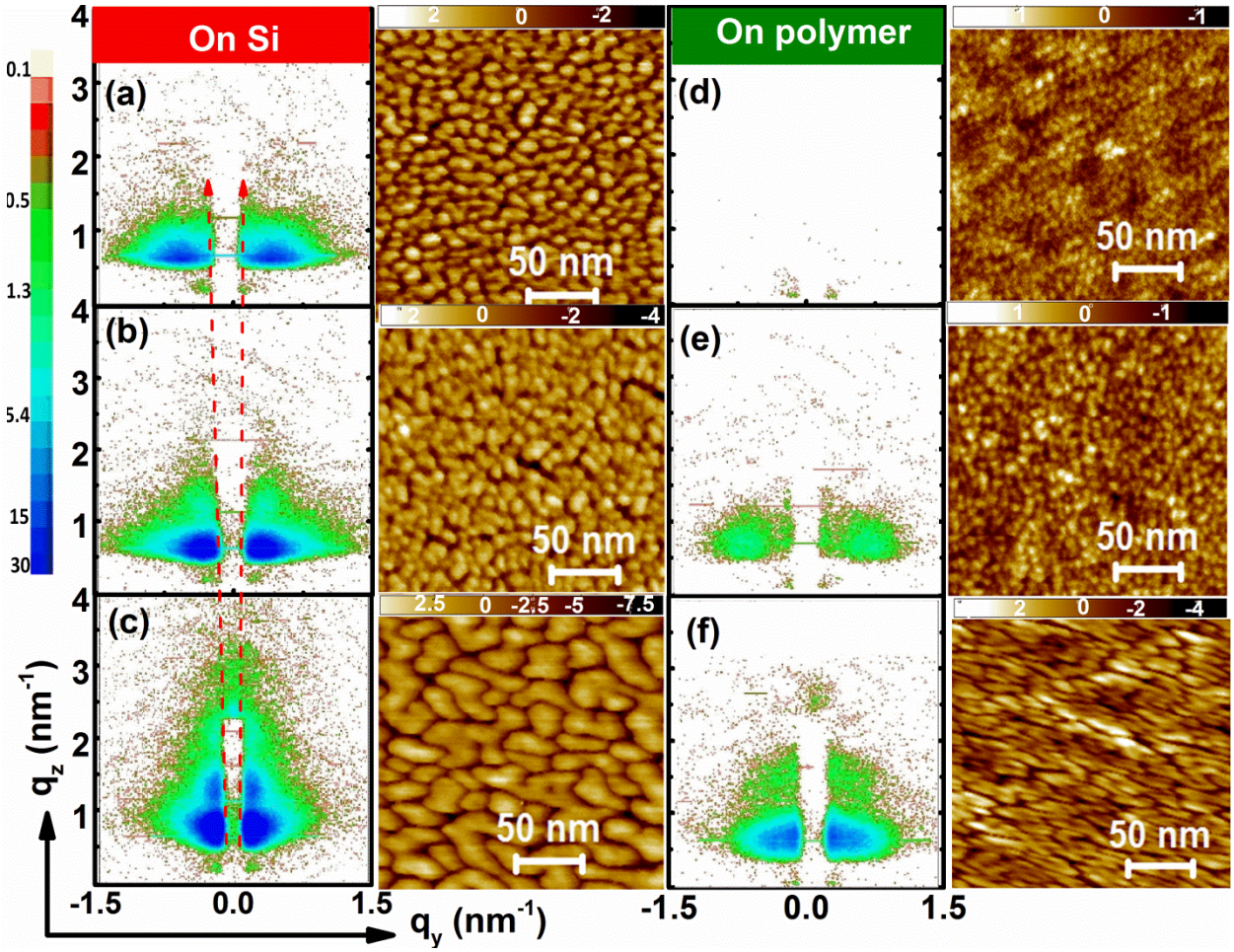

Figure 2: *2D GISAXS patterns and AFM images of gold nanostructures grown on bare Si and polymer-coated Si at few representative growth times, i.e., (a,d) 30, (b, e) 60, and (c, f) 120 s, respectively.*

After 30 s of gold deposition (see Fig. 2(a)) on bare Si, two identical scattering lobes appear in the GISAXS pattern on both sides of the specular plane. The extensions of the scattering lobes parallel or perpendicular to the surface are inversely proportional to the lateral or vertical size of nanostructures in the real space, respectively. These lobes indicate both a well-defined spacing and the dimensions of the surface-grown nanostructures, which can also be seen simultaneously in AFM images. During gold deposition, the distance between the two intensity lobes decreases continuously with increasing coverage, which reveals faster lateral growth and increased particle sizes and inter-particle distances. The uniform shrinkage of intensity lobes at 30 s is indicative of the equal increase of both the in-plane diameter and the height of the round-shaped gold nanostructures. Eventually, coalescence of nanostructures occurs but

continuous films never form, as evident by successive AFM images. Evolution of second-order scattering lobs (Bragg peaks) in the vertical direction of GISAXS patterns (Fig. 2(b–c)) at 60 and 120 s may correspond to the coalescence regime, during which neighboring nanostructures merge to give rise to large flat islands exposing top [111] facets (as shown in Fig. 1, GIXRD results) [22], which are most likely of spinodal type, as shown in the AFM images. Multiple-order peaks are generally exhibited by systems of very concentrated or strongly correlated particles and multilayers [22-24]. Complete coverage is, however, not realized even after long growth times of 15 minutes (not shown), confirming the porous nature of the gold nanofilms.

A similar growth sequence was followed on polymer-coated Si until a percolating thin film of gold was acquired, as shown in Fig 2(d– f). There is hardly any scattering at 30 s, while the scattering pattern of 60 s is similar to the corresponding GISAXS pattern of gold deposited on bare Si at 30 s. This is so because when gold falls on the polymer, it is initially buried in the polymer matrix; with increased growth time this gold nanostructure fill the pores of the polymer and finally rises to the top and covers the polymer surface, thus contributing considerably to the scattering. As a consequence, the second-order scattering lobs evolving in the vertical direction are not highly pronounced (Fig. 2(f)) compared with the case of gold deposited on bare Si (Fig. 2(c)). When gold atoms land on the polymer substrate, some diffuse onto the polymer surface forming aggregates, which act as nucleation seeds initially inside the polymer matrix. Complete coverage of gold was, however, also not realized even after extended growth time (15 minutes).

ii) Quantitative Analysis

Besides qualitative information about the gold-polymer nanointerface, GISAXS maps were quantitatively analyzed by the Guinier [25] and Porod [26] laws in the low ($q \to 0$) and high ($q \to \infty$) scattering ranges, respectively. A comparative surface analysis was also undertaken by using the Height-Height Correlation Function (*HHCF*) [27-29] and Power Spectral Density Function (*PSDF*) [28-30] calculated from AFM images (1×1 μm^2 scan size). These approaches give insight about the spread of heights from a mean plane, and the lateral distance over which the height variations or mutual correlation occur. The *HHCF* is a real-space function and is defined by the statistical average of the mean square of height difference between a pair of points separated by r, and is written as: $HHCF = \langle [h(r + r_0) - h(r_0)]^2 \rangle$, where $h(r + r_0)$ is the height of the surface at relative position r and $h(r_0)$ is the mean surface height. The *HHCF* can be better described by a Gaussian correlation model [28];

$$HHCF = \begin{cases} 2\sigma^2\left[1 - e^{-\left(\frac{r}{\xi}\right)^{2\alpha}}\right] & 0 > r < \infty \\ 2\sigma^2\left(\frac{r}{\xi}\right)^{2\alpha} & r \ll \xi \\ Constant\ (2\sigma^2) & r \gg \xi \end{cases} \qquad \text{Eq. (2),}$$

where ξ is the lateral correlation length which distinguishes short $(r \ll \xi)$ and long $(r \gg \xi)$ range behaviors of rough surfaces, σ is the saturation roughness, and α is the local roughness exponent.

The $log - log$ plots of $HHCF$ vs. r along with a curve fitted to equation (2) are shown in Fig. 3(a) for representative samples (30 and 120 s). As expected, $log(HHCF)$ increases linearly with $log(r)$ for short distances r, demonstrating a power-law behavior ($HHCF \propto r^{2\alpha}$), and saturates to the value of $2\sigma^2$ for larger r, which corresponds to the long-range roughness. All these (σ and ξ) parameters plotted with growth time in Fig. 3(b) have special significance with respect to the surface morphology. The higher $\alpha(\sim 1)$ values for all samples are indicative of in-plane diffusion-dominated growth and locally smooth morphology. ξ corresponds to the largest lateral length in which the height is still correlated. The ξ value increases with growth time from 3 to 7.5 nm in gold films without polymer, as shown in Fig. 3(b), indicating the lateral growth of the gold islands. The lateral growth can also be attributed to an increase in crystallite size of the gold particles [28, 30]. However, the opposite trend is observed on polymer-coated Si, where the value of ξ falls from 9.6 to 3.5 nm, possibly because of increased separation between gold islands. The oscillating behavior of $HHCF$ in the region $r \gg \xi$ indicates formation of aggregates, grain clustering, or mounded structures. The σ values are consistently increasing with growth time for both cases, but their magnitude is small (~1.5 – 2.5 nm). Corresponding 1D scattering intensity (I) vs. scattering vector q (q_y and q_z) curves extracted from 2D GISAXS maps are shown in the Inset of Fig. 3(a) for one of the representative samples. This curve was fitted using the Guinier approximation $[I(q)_{q\to 0} = I(0)\exp\left(-\frac{1}{3}q^2R_g^2\right)]$ to obtain the Guinier radius (R_g) [24]. The R_{gy} (lateral) and R_{gz} (vertical) values vs. growth time are plotted in Fig. 3(c). The average diameters, $\langle D\rangle$, calculated for a spherical shape $\left(2R_g\sqrt{\frac{5}{3}}\right)$ [25], are equal to 5.4 – 11.2 nm when grown on bare Si, which is consistent with AFM results. The difference between R_{gy} and R_{gz} values increases with growth time, and the highest $\frac{R_{gy}}{R_{gz}}$ ratio of 1.5 is obtained at 120 s, which suggests the anisotropic nature of gold nanofacets compared with initially gown round-shaped $\left(\frac{R_{gy}}{R_{gz}} = 1\right)$ nanoparticles. A similar increasing trend in R_{gy} and R_{gz} values can be seen on polymer-coated Si with $\langle D\rangle$ in the range of 6 – 11 nm.

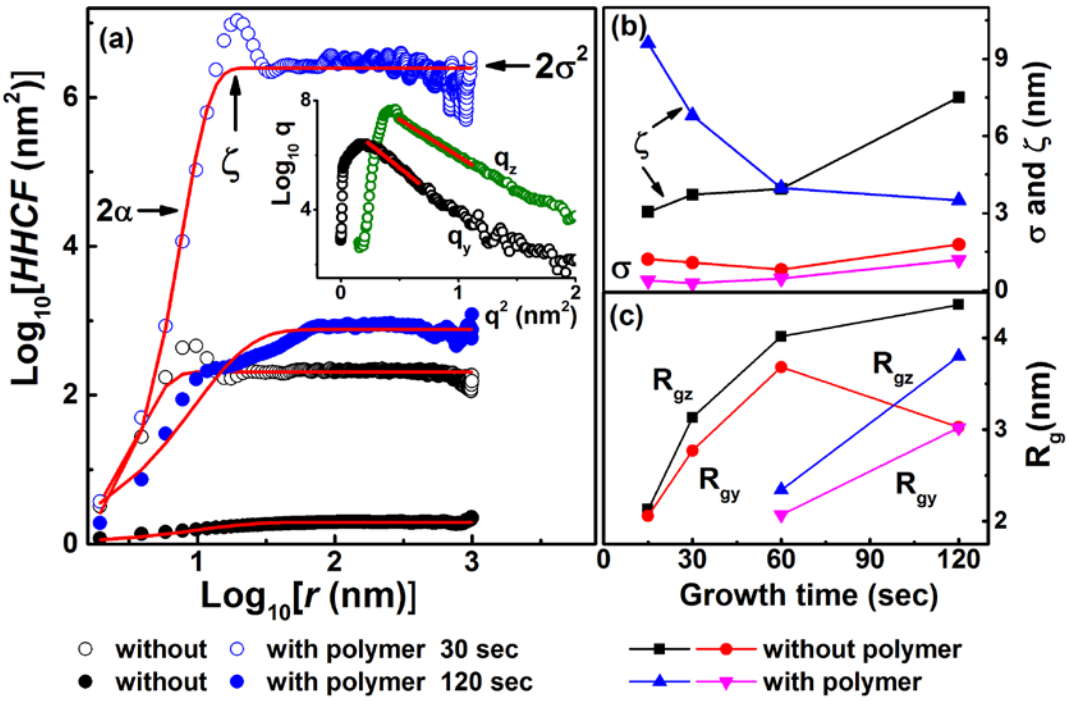

Figure 3: *Log–log plots of HHCF, as a function of distance r and fitted to eqn.* (2) *for two representative samples* (*a*). *Variation in surface roughness σ, correlation length ξ* (*b*), *and Guinier radius R_{gy} and R_{gz} (vertical) values with growth time* (*c*). *1D GISAXS intensity (I) vs. scattering vector q curves fit the Guinier expression at low q regime for a growth time of 30 s* (*Inset* (*a*)).

Alternatively, the dependency of the surface roughness on frequency, f (length^{-1}) can be characterized using the *PSDF* in the reciprocal space. The *PSDF* is calculated as the square of the radially averaged amplitudes of the fast Fourier transform (FFT) [30] of *HHCF* and given by $\frac{1}{2\pi^d}\left|\langle(HHCF)e^{-ifr}\rangle\right|^2$. The $log-log$ plots of the *PSDF* are shown in Fig. 4(a) for the same samples as a function of f=1/r. Generally, experimental curves exhibit flat responses for small values of f and at certain larger values of f they decrease rapidly as a power of the frequency. For a condensed description of gold-polymer morphology, the PSDF curves were fitted into K-correlation (or ABC) model [32-34] expressed by equation (3), which also allows quantitative comparison with *HHCF* parameters.

$$PSDF = A\left[[1+(Bf)^2]^{-C/2}\right] \qquad \text{Eq. (3)}$$

This model provides a knee parameter B which sets the point of transition between low- and high-frequency behavior, constant *PSDF* region at very low values of f, determined by A and at very high

values of f, the surface is fractal determined by C. A is related to a very low f component of roughness and B is the correlation length related to grain size. These parameters are further related to equivalent roughness $\sigma_{eq} = \frac{2\pi A}{B^2(C-1)}$ and correlation length $\xi_{eq} = \frac{(C-1)^2 B^2}{2\pi^2 C}$ [32]. The parameters C and B extracted from fitting are shown in Fig. 4(b) and the Inset of Fig. 4(b), respectively. The B value increases from 0.4 nm to 1.8 nm with growth time on bare Si, while it shows maxima on polymer-coated Si. This is due to the contribution of polymer molecules, as during the initial growth time (15 and 30 s) gold is buried inside the polymer matrix leaving polymer at the surface to be analyzed. These trends are consistent with *HHCF* data of ξ. The *C*-factor decreases for gold nanostructures grown on bare Si from 13 to 2.5, indicating increased fractal surfaces from regular, rounded surfaces. The smaller *C*-factor for gold deposited on polymer-coated Si is indicative of ideal fractal behavior. To complement surface fractal behavior, the Porod approximation $[I(q)_{q\to\infty} = 2\pi S(\Delta\rho)^2 q^{-4}]$ [35] was used to analyze 1D GISAXS scattering curves, as shown for one of the samples in Inset of Fig. 4(a). The slope of fitting lines $log(I(q))\ vs.\ log(q)$, yields the fractal dimensions of rough gold surfaces, which are represented in Fig. 4(c). The Porod slopes of gold grown on bare Si decrease from -4.1 to -3 with growth time, which clearly indicates that the initial particles of spherical shapes are smoother (-4), while, after longer growth times, more rough and complex interfaces (-3) between particles and pores are observed. In contrast, gold grown on polymer-coated Si first shows increasing trends from 60 s (-3.1) to 120 s (-4.9); however, it again decreases at 360 s (-2, data not shown), which infers an initial smoothing of the surface and a subsequent formation of intricate geometry and complex interfaces leading to a rough surface.

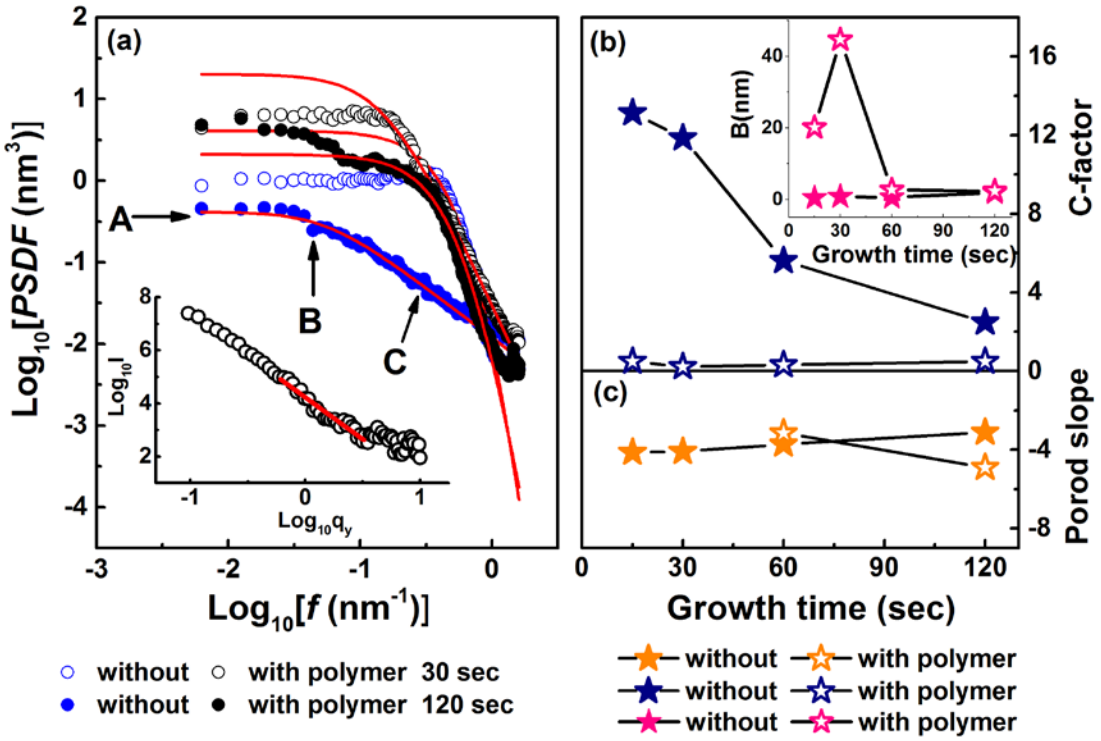

Figure 4: *Log–log plots of PSDF as a function of frequency (=1/r) and fitted to equation* (*3*) *for two representative samples* (*a*). *Variation in parameter B and C* (*b*), *and Porod slope values with growth time.* (*c*). *1D GISAXS intensity (I) vs. scattering* vector *q curves fitted Porod expression at high q regime for growth time of 30 s* (*Inset* (*a*)).

B. Free-Standing Gold-Nanosheets

Free-standing porous gold nanosheets have recently become the rising stars of 2D flatland materials because of their fascinating applications [1-2, 10-12]. Synthesis of free-standing gold nanosheets is significant, but making them dispersible into water solutions without undesired alterations (e.g., aggregation, defects, and adsorption) is a real challenge [1-2, 11-12].

We chemically exfoliated percolating gold nanostructures (grown for 120 s on polymer-coated Si) into water via surface hybridization of gold with bPEI molecules [10]. These micron sized (along two directions) gold sheets preserve their unique free-standing 2D patterns without showing any defects, deterioration, or breakdown, except some bending, as shown by AFM in the Inset of Fig 5(b). The AFM analysis determined that the structures retained smooth, flat, and ultrathin (~7 nm) gold-polymer nanointerfaces. The GISAXS pattern of the gold nanosheet, shown in Fig 5(a), affirms the preserved structure with more resolved X-ray scattering intensity (noise-to-signal ratio) after harvesting, because of

reduced bPEI residues. The 1D GISAXS scattering intensity I vs. q curves (Fig 5(b)) show a shoulder peak along the q_z direction, indicating the preserved gold facets grown in the vertical direction with correlation length $\frac{2\pi}{q_z} = 8.1$ nm [22-24].

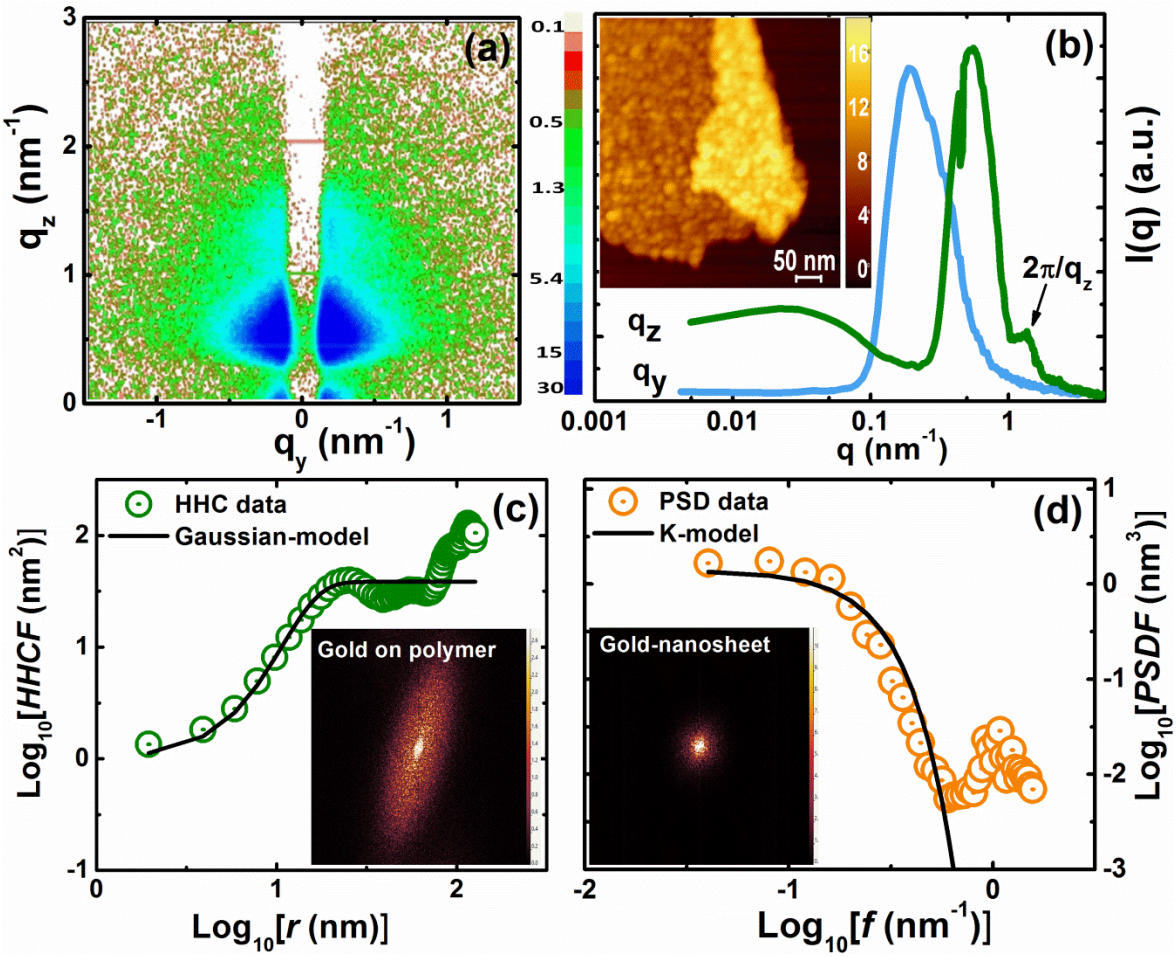

Figure 5: *2D GISAXS patterns of free-standing gold nanosheets* (*a*) *and their 1D scattering intensity* (*I*) *vs. scattering vector, q* (q_y *and* q_z) *curves* (*b*). *The inset of* (*b*) *shows an AFM image of gold nanosheets. HHCF* (*c*) *and PSDF (d) data as a function of length and frequency, and corresponding fitting data of Gaussian and K-model. Insets in* (*c*) *and* (*d*) *show 2D FFT patterns of the AFM images of gold nanosheet and gold deposited at polymer-coated Si at 120 s, respectively.*

Guinier radii (R_{gy} and R_{gz}) approximated using these curves are given in Table 1, indicating the anisotropic nature ($\frac{R_{gy}}{R_{gz}} = 2.46$) of gold in nanosheets. The Porod slope (-1.71) is an indicator of the

rough surfaces of gold nanosheets. The GISAXS pattern of free-standing gold nanosheets resembles the GISAXS pattern of as-grown gold on bare Si at 120 s (see Fig.2(c)). Often, free-standing 2D nanosheets have similar structures as the parent material with slight in-plane expansion and, eventually, a change in symmetry which can be clearly observed in Table 1. Porosity, which is a measure of void spaces in a material, is given by $P = \frac{1}{4\pi^2}\int_0^\infty qI(q)dq$ [36]. The P value for gold nanosheets, estimated by the area under the curve of the $qI(q)$ vs. q plot, was found to be 18.78 %. This indicates their porous nature; P is slightly higher than that of gold nanostructures grown directly on Si. The Gaussian and K-model were also used to determine the useful growth parameter of gold nanosheets from *HHCF* and *PSDF* data, as shown in Fig 5(c) and 5(d), respectively, giving a surface roughness of $\sigma = 0.9$ nm and a lateral correlation length of $\xi = 10.6$ nm. The K-model parameters [A (4.84 nm^2), B (15.4 nm), and C (3.17)] are in good agreement with pure gold (deposition at 120 s), retaining fractal behavior [34]. Further, the *HHCF* is oscillatory in nature for mounded surfaces, which is clearly visible at large *r*; however, the sudden increase of *HHCF* value at the end of the curve is attributed to the folding of gold nanosheets – a similar effect can be seen in *PSDF* at very low f [28,31]. Finally, 2D FFT patterns of AFM images change from a diffuse spot to a bright ring-like structure in f-space [Inset Fig. 5(c) and 5(d)] when gold nanosheets are ditched from beneath the polymer-coated Si substrate, hinting further at the mound growth [28]. The formation of mounds on any surface are basically due to different growth effects such as step-edge barrier, or diffusion at longer growth time which could be local or non-local in nature [28,31].

Table 1: *Guinier radii (R_{gy} and R_{gz}), Porod slope, and porosity estimated from 1D GISAXS scattering curves for free-standing gold nanosheets compared with gold grown on Si and polymer-coated Si.*

Sample (grown at 120 s)	R_{gy} (nm)	R_{gz} (nm)	Porod slope	P (%)
Without Polymer	8.91	22.22	-1.73	15.48
With Polymer	11.45	24.64	-2.14	10.25
2D Nanosheet	9.00	17.63	-1.74	18.78

Additionally, these nanosheet dispersions do not exhibit any shape changes under specific conditions (e.g., pH), in contrast to the “near-percolating” Au-based nanosheets grown at 60 s. Thus, we could not only control the nanoscale growth regime to design the shape-stable free-standing nanosheets over 120 s of deposition time, but also enhance the analytical precision of buried surface structures inside polymer substrates by GISAX and AFM.

C. Gold-Nanorods by Oblique Sputtering

The production of anisotropic gold nanorods is regarded as a significant challenge due to the tendency of metal atoms to form a highly isotropic 3D close-packed crystal lattice. However, growth of anisotropic gold nanorods with high aspect ratio can be obtained at oblique sputter condition (substrate tilted at an angle of 89°) [37]. Just like free-standing gold nanosheets, these nanorods can be exfoliated; thus, the investigation of surface area, growth stability, and intercolumnar spacing by GISAXS is crucial for determining the growth mechanism of gold nanorods on polymer-coated Si substrates.

Formation of well-defined gold nanorods was observed only in a narrow growth window of deposition times between 3-15 minutes at oblique sputter condition; otherwise, mostly flat 2D gold nanoassembly-type structures emerge. GISAXS patterns were measured by in-plane rotation of nanorod samples from 0° to 360° as shown in Fig. 6 (a)-(c) for two representative samples (3 and 15 min). These patterns are quite different in perpendicular directions, while samples at 0° have symmetry about the q_z axis and samples at 90° skew along the q_y axis, which shows that the deposition is oblique [37]. Comparing 3 and 15 min samples at 90°, we can observe that the scattering is narrow in the q_y direction and longer in the q_z direction for the 3 min case, which indicates that nanorods are longer in the vertical direction and occupy less area in the horizontal plane. In contrast, for the 15 min case the scattering pattern looks more rounded, specifying a further elongation of nanorods against their horizontal spreading. The Guinier approximation of $I(q)$ vs. q_y *or* q_z curves at 90° (see Fig. 6(b)-6(d)) gives an idea of the thin nanorods' lengths $L\left(=\sqrt{12}\,R_g\right)$ of ~ 32 nm and ~ 53 nm in the vertical direction with increasing growth time from 3 to 15 min. The corresponding L values for 0° are approximated to ~ 27 and ~ 41 nm. Interestingly, $I(q)$ vs. q_y of the 3 min sample shows a shoulder peak which confirms the extended projections and provides the lateral correlation length values, $D = \frac{2\pi}{q_y}$, between nanorods: 12 (at 0°) and 15 nm (at 90°). There is a difference in D values only because when the deposition is viewed along the 90° direction, the oblique growth regimes tend to occupy more surface area on the substrate, which, in turn, affects the spacing between nanorods. Finally, these oblique-deposited samples show larger porosity values of 18 % (3 min) and 14 % (15 min) than in-plane samples, confirming the larger spacing between the structures, which is the primary property of the nanorods occupying less horizontal area. In a similar fashion, when gold was obliquely deposited directly on Si from 3 to 15 min (shown in the Supporting Information, Figure S2), the porosity became 42 - 54 %, which is a threefold increase compared with that of in-plane samples. Also, the well-separated nanorods can be better grown on polymer coated Si in comparison to bare Si, because polymer appears to act as a mold that shapes

nanorods rather than spreading gold in the lateral direction. Thus, these variations in physical geometry end up altering properties like absorption or mechanic-optoelectronic properties, which primarily depend on rough surfaces and gold-polymer interfaces [6-7].

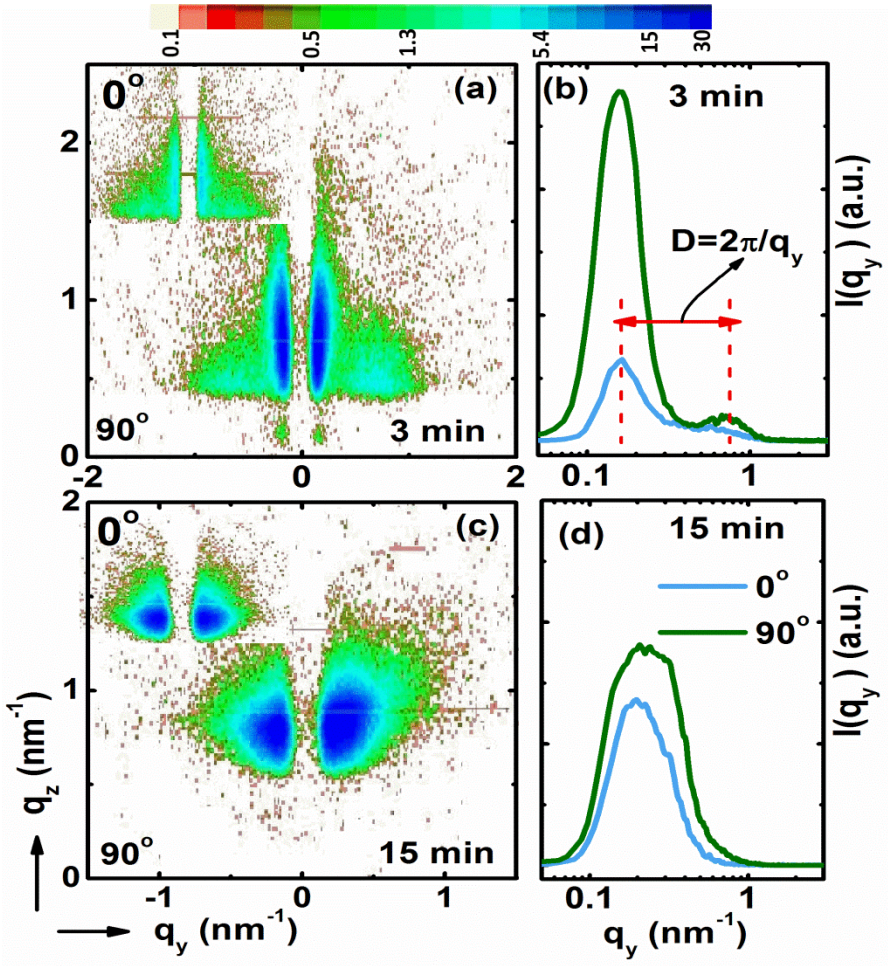

Figure 6. *2D GISAXS patterns measured at mutually perpendicular directions (*0º and 90º*) for oblique deposition of gold nanorods on polymer-coated Si for 3 min* (*a*) *and 15 min* (*c*)*. Corresponding 1D scattering intensity* (*I*) *vs.* q_y *curves* (*b and d*)*.*

Conclusions: Gold-polymer composites can lead to a new family of functional materials with tunable collective properties. However, to fully exploit the polymers' ability to control aggregation in order to fabricate flexible yet mechanically robust materials, it is important to achieve a deep understanding of gold-polymer interfaces. In this article, we correlate the morphology of various gold nanostructures synthesized either on polymer-coated Si or directly on Si substrates with in-plane or oblique sputtering geometry. From a unique combination of GISAXS and AFM analysis, we followed the morphology

development of the gold nanostructures with selected thicknesses and identified the main growth kinetic regimes as well as their thresholds, which is crucial for tailoring nanostructures. Utilization of lab-based GISAXS was clearly demonstrated; moreover, the presented analysis could be applied not only on diverse gold nano-island decorated surfaces but also on 2D free-standing gold nanosheets after exfoliation. Further, a comparative analysis of *HHCF* and *PSDF* obtained from AFM images, and Guinier and Porod approximation of GISAXS data proposed possible growth mechanisms quantitatively.

Acknowledgment: We are grateful to Prof. Mukhles Sowwan for providing experimental facilities. We thank Dr. J.-H. Kim for polymerization of substrates. We also thank Mr. C. Ruhathia for running AFM image analysis software.

References:

1) G.–H. Lim, S. S. Kwak, N. Kwon, T. Kim, H. Kim, S. M. Kim, S.–W. Kim, B. Lim, Fully stretchable and highly durable triboelectric nanogenerators based on gold-nanosheet electrodes for self-powered human-motion detection, Nano Energy 42(2017)300-306. https://doi.org/10.1016/j.nanoen.2017.11.001.
2) G.–H. Lim, N. E. Lee, B. Lim, Highly sensitive, tunable, and durable gold nanosheet strain sensors for human motion detection, J. Mater. Chem. C 4(2016)5642-5647. https://doi.org/10.1039/C6TC00251J.
3) T. E. Glier, L. Akinsinde, M. Paufler, F. Otto, M. Hashemi, L. Grote, L. Daams, G. Neuber, B. Grimm-Lebsanft, F. Biebl, D. Rukser, M. Lippmann, W. Ohm, M. Schwartzkopf, C. J. Brett, T. Matsuyama, S. V. Roth, M. Rübhausen, Functional printing of conductive silver-nanowire photopolymer composites, Sci. Rep. 9(1) (2019)6465. https://doi.org/10.1038/s41598-019-42841-3.
4) F. Rossi, N. T. K. Thanh, X. D. Su, Gold nanorods embedded in polymeric film for killing bacteria by generating reactive oxygen species with light, ACS Applied Bio Materials *2*(7) (2019)3059-3067. doi: 10.1021/acsabm.9b00343.
5) M. Mirigliano, D. Decastri, A. Pullia, D. Dellasega, A. Casu, A. Falqui, P Milani, Complex electrical spiking activity in resistive switching nanostructured Au two-terminal devices, Nanotechnology 31(23)(2020)234001. https://doi.org/10.1088/1361-6528/ab76ec.
6) H. A. Nguyen, P. Banerjee, D. Nguyen, J. W. Lyding, M. Gruebele**,** P. K. Jain**,** STM imaging of localized surface plasmons on individual gold nanoislands, J. Phys. Chem. Lett. 9(8)(2018)1970-

1976.
https://doi.org/10.1021/acs.jpclett.8b00502.

7) N. Bhalla, A. Jain, Y. Lee, A. Q. Shen, D. Lee, Dewetting metal nanofilms—effect of substrate on refractive index sensitivity of nanoplasmonic gold, Nanomaterials 2019, 9(11), 1530. https://doi.org/10.3390/nano9111530.
8) C. Minnai, M. Di Vece, P. Milani, Mechanical-optical-electro modulation by stretching a polymer-metal nanocomposite, Nanotechnology 28(35)(2017)355702. https://doi.org/10.1088/1361-6528/aa7c07.
9) C. Minnai, M Mirigliano, S. A. Brown, P Milani, The nanocoherer: an electrically and mechanically resettable resistive switching device based on gold clusters assembled on paper, Nano Futures 2 (1) (2019) 011002. https://doi.org/10.1088/2399-1984/aab4ee.
10) J.-H. Kim, M. Bohra, V. Singh, C. Cassidy, and M. Sowwan, Smart composite nanosheets with adaptive optical properties, ACS Applied Materials and Interfaces 6(2014)13339-13343. https://doi.org/10.1021/am5041708.
11) S. Ye, A. P. Brown, A. C. Stammers, N. H. Thomson, J. Wen, L. Roach, R. J. Bushby, P. L. Coletta, K. Critchley, S. D. Connell, A. F. Markham, R. Brydson, S. D. Evans, Sub-nanometer thick gold nanosheets as highly efficient catalysts, Advance Science 6(21)(2019)1900911. https://doi.org/10.1002/advs.201900911.
12) V. Kumar, Y.-J. Park, B. V. Reddy, A. F. Wu, Synthesis of single-crystalline gold nanosheet having multilayer structure under the polymeric bulk condition, Applied Mechanics and Materials 548-549(2014)301-304. https://doi.org/10.4028/www.scientific.net/AMM.548-549.301.
13) J.-J. Song, R. Bhattacharya, H. Kim, J. Chang, T.-Y. Tang, H. Guo, S. K. Ghosh, Y. Yang, Z. Jiang, H. Kim, T. P. Russell, G. Arya, S. Narayanan, and S. K. Sinha, One-dimensional anomalous diffusion of gold nanoparticles in a polymer melt, Phys. Rev. Lett.122(2019)107802. https://doi.org/10.1103/PhysRevLett.122.107802.
14) A. Hexemer, P. Muller-Buschbaum, Advanced grazing-incidence techniques for modern soft-matter materials analysis, IUCrJ.2 (1) (2015)106-125. doi: 10.1107/S2052252514024178.
15) M. Schwartzkopf and S. V. Roth , Investigating polymer–metal interfaces by grazing incidence small-angle X-ray scattering from gradients to real-time studies, Nanomaterials 6(12)(2016)239. https://doi.org/10.3390/nano6120239.

16) G. Renaud, R. Lazzari, F. Leroy, Probing surface and interface morphology with grazing incidence small angle X-ray scattering, Surface Science Reports 64(2009)255-380. https://doi.org/10.1016/j.surfrep.2009.07.002.

17) E. Metwalli, S. Couet, K. Schlage, R. Röhlsberger, V. Körstgens, M, Ruderer, W. Wang, G. Kaune, S. V. Roth, P. Müller-Buschbaum, In situ GISAXS investigation of gold sputtering onto a polymer template, Langmuir 24(2008)4265-4272. https://doi.org/10.1021/la7038587.

18) M. Schwartzkopf, A. Buffet, V. Körstgens, E. Metwalli, K. Schlage, G. Benecke, J. Perlich, M. Rawolle, A. Rothkirch, B. Heidmann, G. Herzog, P. Müller-Buschbaum, R. Röhlsberger, R. Gehrke, N. Stribeck, S. V. Roth, From atoms to layers: *in situ* gold cluster growth kinetics during sputter deposition, Nanoscale 5(2013)5053-5062. https://doi.org/10.1039/C3NR34216F.

19) T. Narayanan, O. Konovalov, Synchrotron scattering methods for nanomaterials and soft matter research, Materials 13(3) (2020)752. https://doi.org/10.3390/ma13030752.

20) P. Zhang, B. Reiser, L. González-García, S. Beck, J. Drzic, T. Kraus, Drying of electrically conductive hybrid polymer-gold nanorods studied with in situ microbeam GISAXS, Nanoscale 11(14)(2019)6538-6543. https://doi.org/10.1039/C8NR09872G.

21) D. Dong, L. W. Yap, D. M. Smilgies, K. J. Si, Q. Shi, W. Cheng, Two-dimensional gold trisoctahedron nanoparticle superlattice sheets: self-assembly, characterization and immunosensing applications, Nanoscale10(2018)5065-5071. https://doi.org/10.1039/C7NR09443D.

22) N. Jedrecy, G.Renaud, R. Lazzari, J. Jupille, Flat-top silver nanocrystals on the two polar faces of ZnO: An all angle x-ray scattering investigation, Phys. Rev. B72(2005)045430. https://doi.org/10.1103/PhysRevB.72.045430.

23) H. Okuda and S. Ochiai, Grazing-incidence small-angle scattering measurement of Ge islands capped with a Si layer, Appl. Phys. Lett. 81(2002)2358. https://doi.org/10.1063/1.1509112.

24) B. Pivac, P. Dubček, I. Capan, H. Zorc, J. Dasović, S. Bernstorff, M. Wu, B. Vlahovic, GISAXS study of Si nanostructures in SiO_2 matrix for solar cell applications, Physica Status Solidi (a), 210(2013)755-759. https://doi.org/10.1002/pssa.201200527.

25) A. Guinier, La diffraction des rayons X aux très petits angles: application à l'étude de

phénomènes ultramicroscopiques, Annals of Physics, 12(1939)161-237. https://doi.org/10.1051/anphys/193911120161

26) K. Hoydalsvik, T. Barnardo, R. Winter, S. Haas, D. Tatchev, A. Hoell, Yttria-zirconia coatings studied by grazing-incidence small-angle X-ray scattering during *in situ* heating Phys. Chem. Chem. Phys. 12, (2010)14492-14500. https://doi.org/10.1039/C0CP00472C.

27) J. K. Bal, S. Hazra, Interfacial role in room-temperature diffusion of Au into Si substrates, Physical Review B 75(20) (2007)205411. https://doi.org/10.1103/Phys.RevB.75.205411.

28) R. Kesarwani, P. P. Dey and A. Khare Correlation between surface scaling behavior and surface plasmon resonance properties of semitransparent nanostructured Cu thin films deposited via PLD**,** RSC Adv. 9(2019)7967-7974. https://doi.org/10.1039/C9RA00194H.

29) A. S. Meshkova, S. A. Starostin, M. C. M. van de Sanden, H. W. de Vries, Variable roughness development in statically deposited SiO_2 thin films: a spatially resolved surface morphology analysis, J. Phys. D: Appl. Phys. 51 (2018)285303. https://doi.org/10.1088/1361-6463/aacb1c.

30) T. Hesjedal, J. Mohanty, F. Kubat, W. Ruile and L. M. Reindl, A microscopic view on acoustomigration, IEEE Transactions on Ultrasonics, Ferroelectrics, and Frequency Control 52(9)(2005)1584-1593. DOI:10.1109/TUFFC.2005.1516031.

31) S. M. Obaidulla, P. K. Giri, Surface roughening and scaling behavior of vacuum-deposited $SnCl_2Pc$ organic thin films on different substrates, Applied Physics Letters 107(2015)221910. http://dx.doi.org/10.1063/1.4936937.

32) Y. Gong, S. T. Misture, P. Gao, N.P. Mellott, Surface roughness measurements using power spectrum density analysis with enhanced spatial correlation length, J. Phys. Chem. C, 120(39)(2016)22358–22364. https://doi.org/10.1021/acs.jpcc.6b06635.

33) S. Karan and B. Mallik, Power spectral density analysis and photoconducting behavior in copper(II) phthalocyanine nanostructured thin films, Phys. Chem. Chem. Phys.10(2008)6751–6761. DOI: 10.1039/b809648a.

34) F. M. Mwema, O. P. Oladijo, T. S. Sathiaraj, E. T. Akinlabi, Atomic force microscopy analysis of surface topography of pure thin aluminum films, Mater. Res. Express

5(2018)046416.
https://doi.org/10.1088/2053-1591/aabe1b.

35) S. Lenz, M. Bonini, S. K. Nett1, M. C. Lechmann, S. G. J. Emmerling, R. S. Kappes, M. Memesa, A. Timmann, S. V. Roth, J. S. Gutmann, Global scattering functions: a tool for grazing incidence small angle X-ray scattering (GISAXS) data analysis of low correlated lateral structures, Eur. Phys. J. Appl. Phys. 51(2010)10601.
DOI: 10.1051/epjap/2010064.

36) L. L. Yang, D. T. Ge, X. D. He, F. He, Y. B. Li, S. Zhang, Grazing incidence X-ray scattering study of sol–gel derived indium tin oxide thin films, Thin Solid Films, 517 (2009)5151-5156.
https://doi.org/10.1016/j.tsf.2009.03.047.

37) R. Alvarez, J. M. García-Martín, M. Macías-Montero, L. Gonzalez-Garcia, J. C. González, V. Rico, J. Perlich, J. Cotrino, A. R. González-Elipe, A. Palmero, Growth regimes of porous gold thin films deposited by magnetron sputtering at oblique incidence: from compact to columnar microstructures, Nanotechnology 24(4)(2013)045604.
https://doi.org/10.1088/0957-4484/24/4/045604.